

Spectroscopic characterization of H_2 and D_2 helicon plasmas generated by a resonant antenna for neutral beam applications in fusion

C. Marini¹, R. Agnello¹, B.P. Duval¹, I. Furno¹, A.A. Howling¹, R. Jacquier¹, A.N. Karpushov¹, G. Plyushchev¹, K. Verhaegh¹, Ph. Guittienne², U. Fantz³, D. Wunderlich³, S. Béchu⁴ and A. Simonin⁵

¹ EPFL, Swiss Plasma Center (SPC), CH-1015 Lausanne, Switzerland

² Helyssen, Route de la Louche 31, CH-1092 Belmont-sur-Lausanne, Switzerland

³ Max-Planck-Institut für Plasmaphysik, Boltzmannstr. 2, 85748 Garching, Germany

⁴ LPSC, Université Grenoble-Alpes, CNRS/IN2P3, F-38026 Grenoble, France

⁵ CEA, IRFM, F-13108 St Paul lez Durance, France

E-mail: claudio.marini@epfl.ch

Received 16 September 2016, revised 4 December 2016

Accepted for publication 14 December 2016

Published 30 January 2017



Abstract

A new generation of neutral beam systems will be required in future fusion reactors, such as DEMO, able to deliver high power (up to 50 MW) with high (800 keV or higher) neutral energy. Only negative ion beams may be able to attain this performance, which has encouraged a strong research focus on negative ion production from both surface and volumetric plasma sources. A novel helicon plasma source, based on the resonant birdcage network antenna configuration, is currently under study at the Swiss Plasma Centre before installation on the Cybele negative ion source at the Institute for Magnetic Fusion Research, CEA, Cadarache, France. This source is driven by up to 10 kW at 13.56 MHz, and is being tested on a linear resonant antenna ion device. Passive spectroscopic measurements of the first three Balmer lines α , β and γ and of the Fulcher- α bands were performed with an $f/2$ spectrometer, for both hydrogen and deuterium. Multiple viewing lines and an absolute intensity calibration were used to determine the plasma radiance profile, with a spatial resolution <3 mm. A minimum Fisher regularization algorithm was applied to obtain the absolute emissivity profile for each emission line for cylindrical symmetry, which was experimentally confirmed. An uncertainty estimate of the inverted profiles was performed using a Monte Carlo approach. Finally, a radiofrequency-compensated Langmuir probe was inserted to measure the electron temperature and density profiles. The absolute line emissivities are interpreted using the collisional-radiative code YACORA which estimates the degree of dissociation and the distribution of the atomic and molecular species, including the negative ion density. This paper reports the results of a power scan up to 5 kW in conditions satisfying Cybele requirements for the plasma source, namely a low neutral pressure, $p \leq 0.3$ Pa and magnetic field $B \leq 150$ G.

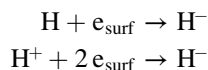
Keywords: neutral beam injection, DEMO, negative ion source, helicon source

(Some figures may appear in colour only in the online journal)

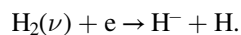
1. Introduction

The heating scheme for future fusion reactors such as DEMO relies on multiple actuators, among which neutral beam (NB) systems play a major role [1]. In order to reach the core region, the NBs must have high energy (~ 800 keV or higher). At the same time, to effectively heat the plasma, high (up to 50 MW) powers are necessary. Most NBs are currently based on positive ion sources that have been developed for high reliability and ease of maintenance. After acceleration to the desired energy, the positive atoms are neutralized by charge exchange reactions with a neutral gas. However, the neutralization efficiency of positive ions decreases drastically above 100 keV amu^{-1} [2], prohibiting their use for high particle energy NBs. Conversely, the gas neutralization (in reality ionisation) efficiency of negative ions remains essentially constant above 100 keV amu^{-1} , with typical values of 60%; other more efficient methods that can exceed 80%, such as photodetachment, can also be implemented [3]. Current negative ion sources supply negative ion densities one order of magnitude lower than those of positive sources, which has led to a strong research and development effort on alternative negative ion sources. The requirements on such sources are stringent. For example, in DEMO the target extraction current density is 200 A m^{-2} , the pressure 0.2 Pa, the pulse duration up to 2 h and the extraction area 0.1 m^2 , with a beam uniformity of $\pm 10\%$ and a co-extracted electron fraction < 1 . The last requirement is particularly challenging due to the higher mobility of electrons compared with negative ions. The generation of negative hydrogen or deuterium (represented throughout this paper by the character H when referring to both) ions is based on two processes [2]:

- (i) surface production, where negative ions are the result of the interaction of a neutral H atom or an ion H^+ with a low work function surface:



- (ii) volumetric production, where the negative ions are produced by dissociative attachment (DA) of electrons to molecules that are in an excited ro-vibrational level ν :



Most present-day efforts to develop new negative ion sources focus on surface production, using caesium for its low surface work function. For example, filament arc sources [4] and radiofrequency (RF) sources [5]. Recently, it was proposed to use a helicon plasma source because of its high ionization efficiency [6], (particularly at low pressures) and its volumetric ion production. The cross section for DA production is strongly dependent on the molecular vibrational level ν . It increases by four orders of magnitude from $\nu = 0$ to $\nu = 4$ [2]. A highly vibrationally excited molecular population requires relatively high electronic energies ≥ 10 eV, as the radiative decay of excited electronic states, known as E–V singlet excitation [2], is an effective source of vibrationally excited molecules. This mechanism is responsible for the peak in DA cross

section at ≈ 14 eV [7, 8]. T_e must, however, be kept below 2 eV to reduce H^- detachment from electronic collisions, which is a very effective process due to the low binding energy (0.75 eV) of the extra captured electron [9]. To fully understand the mechanism behind negative ion production complete characterization of the electron energy distribution function (EEDF) may therefore be required, especially for helicon sources, which have revealed, under certain conditions, the presence of non-Maxwellian features [10, 11]. An extension of the present investigation to measure the detailed EEDF in resonant antenna ion device (RAID) plasmas will be the subject of future work. For the purpose of this paper a Maxwellian EEDF was assumed. Negative ion volumetric production in helicon plasmas is efficient, with a high-temperature electron population confined by the magnetic field in the plasma-producing region and a low-temperature population diffused over a larger area, which provides the electrons for DA whilst reducing collisional losses. The main disadvantage of volumetric production compared with surface production for negative ion beam applications is the higher co-extracted electron fraction. It is also not proven yet whether volumetric processes could produce the same quantity of negative ions as surface conversion at low pressure.

This paper focuses on the characterization of the helicon resonant birdcage network antenna recently developed at the Swiss Plasma Centre for application as negative ion source in the source NB test Cybele [3]. The experimental setup is described in section 2, with emphasis on the spectroscopic system. Section 3 explains in detail the steps used to compute the emissivities from the measured spectra, which are interpreted in section 4 to estimate the density of ions and neutral atoms. Emphasis is given to the degree of dissociation, the degree of ionization and the negative ion density. The results are discussed in section 5 and the conclusions and outlook are illustrated in section 6.

2. RAID experimental setup and spectroscopic system

The reported optical emission spectroscopy (OES) measurements are performed in the RAID shown in figure 1, where the antenna and the input optics for OES are highlighted. The vacuum chamber is cylindrical, with a length of 1.8 m and a diameter of 0.4 m. The RAID is equipped with six magnetic field coils able to generate an axial magnetic field up to 800 G. A coil current $I_{\text{coil}} = 150$ A provides an axial B field in the vacuum chamber axis of 150 G, which meets the specifications of the Cybele source [3]. The current of the first coil next to the antenna is reversed, $I_{\text{coil}} = -30$ A, which increases the B gradient to give better antenna performance [6, 12]. The pressure is controlled by the gas inflow through a Bronkhorst mass flow controller at constant pumping speed and is monitored by a Balzers pressure gauge. The pressure of 0.3 Pa, also required for operation in Cybele, is attained with a flow of $7.5 \text{ ml}_n \text{ min}^{-1}$. This relatively low gas pressure is one of the source requirements for ITER NBs, the purpose of which is to minimize the negative ion losses due to

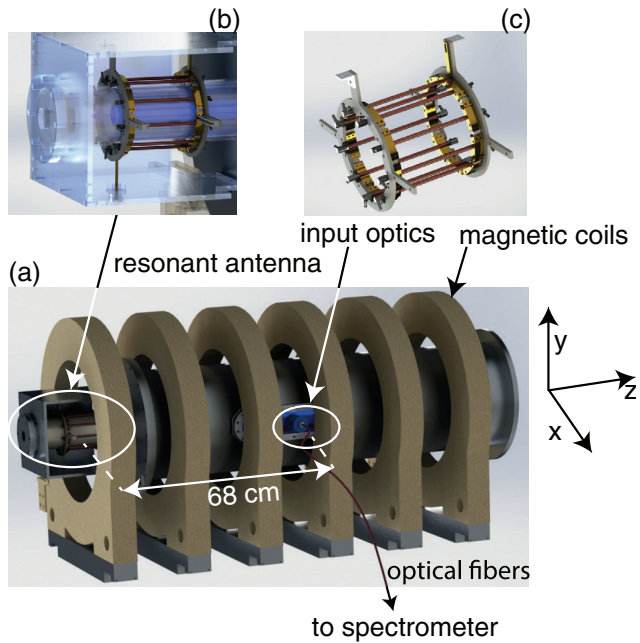


Figure 1. Computer-aided design of (a) RAID and the helicon resonant antenna (b) and (c). The device has a circular cross section of diameter 0.4 m and a length of 1.8 m. The input optics for optical emission spectroscopy measurements are mounted on a port ~ 68 cm from the resonant antenna.

collisions with molecules in the accelerator. Pressure variations are limited to $<20\%$ during the measurements. The antenna (see figures 1(b) and (c)) is designed to efficiently couple with the plasma helicon wave field for modes $m = \pm 1$ [13]. It has nine straight copper rods 15 cm long, an internal diameter of 13 cm and a single RF power injection. It contains 16 high-current, high- Q , non-magnetic capacitors, each with a capacitance of 3.96 nF. The antenna, able to deliver up to 10 kW at the standard ISM frequency of 13.56 MHz, is installed at one end of RAID, outside the main coil region, as shown in figure 1(a). The plasma generated by the antenna forms a column of approximately constant radius that ends on a target at the other end of the device.

The spectroscopic setup consists of a field lens coupled through an optical fibre bundle to a high-throughput spectrometer and a detector. The input optics is a Navitar $f/1.4$ 35 mm lens and the image focal plane is optimized to image the RAID axis at 25 cm from the lens. The input lens is mounted on a port about 68 cm from the antenna to sample the plasma column far from the source. The fibre bundle is composed of 19 fibres of numerical aperture 0.22, with a fused silica core of diameter 365 μm . The diameter of their adjacent images on the focal plane is 2.9 mm, resulting in a 55.1 mm wide sampling region. The geometry of the lines of sight (LOS) is shown in figure 2(a), together with a sketch of the RAID cross section. A violet inner ring schematically represents the position of the plasma column. The figure also defines the impact parameter p for a LOS, i.e. the distance of the LOS from the centre of the plasma column, and the radius r for a generic point, i.e. the distance of the point from the device axis. In a RAID, the centre of the plasma column coincides with the mechanical axis. A core observation set that views

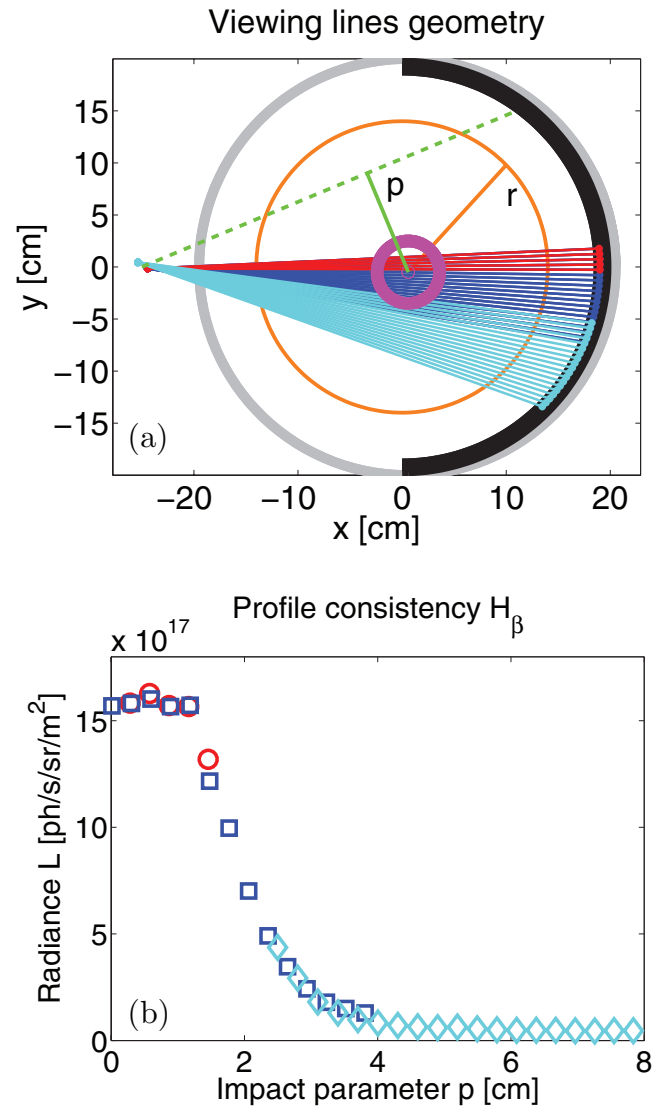


Figure 2. (a) Line of sight (LOS) for the two sets of measurements. Red and blue lines corresponds to the core measurements above and below the plasma column centre, respectively. Cyan shows the LOS for the edge set. The plasma column is schematically represented by a violet circle. The dashed green line simulates a LOS for the definition of the impact parameter p . The orange circle is used to define the radius r from the device axis. (b) Profile consistency check (same colours as in (a)), the cylindrical symmetry and the connection of the core and edge set are verified.

the plasma column and an edge set that focuses on the outer region are available. Core LOS view the plasma column both above and below its centre and are represented by red and blue lines, respectively. Their goal is to ascertain the cylindrical symmetry of the plasma column emission. The edge measurements set observes impact parameter ranges up to 8 cm and partially overlaps with the core set, so that the consistency across the set merge region can be assessed as shown in figure 2(b), where $n_{\text{LOS}} = 38$ LOS are displayed. The LOS geometry was verified by back illuminating each fibre with a He/Ne laser and measuring the projected spot position on a reference anti-reflection graphite ring installed inside the vacuum vessel, represented by a black semicircle in figure 2(a).

Collected light is analysed by a high-throughput spectrometer of similar design to [14]. It is composed of two Nikon $f/2$ 200mm lenses and a Horiba holographic grating of 2400 l mm^{-1} groove density blazed at 400nm. The clear aperture of the Nikon lenses is 100mm and a grating of size $120 \times 140 \text{ mm}^2$ was chosen to minimize vignetting. The angle between the optical axis of the two lenses was fixed to $2\phi = 20^\circ$, where ϕ is the half-included angle. The angle θ between the bisector of the two lenses and the grating normal, called the scanning angle, is adjustable and determines the central wavelength. The spectrometer spectral coverage is $\sim 14 \text{ nm}$ and is too small to cover all the lines of interest within a single exposure. A set of eight scanning angles, that include a partial overlap in the Fulcher- α range between 600 and 650nm, was used. This method is viable only if the emission of all lines is stable in time for the whole scan, an assumption that was verified by repeating the full angular scan at least twice for each antenna power. A constant emissivity (within 5%) is observed within a few seconds for each input power value. The input slit width of the spectrometer was set to $80 \mu\text{m}$ for a spectral bandpass of 0.9 \AA at 615nm. This is sufficient to resolve most of the Fulcher- α molecular lines. The spectrometer uses an Andor iXon Ultra 897 camera, which features a back-illuminated 512×512 pixel frame transfer sensor and an optional electron multiplying (EM) readout register. The camera integration time and EM gain are adjusted at each scanning angle and power to maximize the counts and signal-to-noise ratio whilst avoiding saturation. The allowed integration time is in the range 3.5×10^{-4} – 0.2 s where EM gains between 8 and 60 were employed. A complete spectrum is the result of an average of 15–30 of such acquisitions, with the experimental uncertainty estimated from the inter-spectra standard deviation. Figure 3 shows a spectrum of the H_2 Fulcher- α 22QN lines for different RF powers, obtained with the procedure described above.

3. Absolute radiance measurements and emissivity profiles

We now describe the procedure to calculate absolute line emissivity. It consists of two steps: a radiance calculation from the measured spectra and the tomographic inversion of these radiance profiles. The experiments were performed at a constant pressure of 0.3 Pa, in both hydrogen and deuterium. A scan in the antenna input power was performed for both isotopes but with a different power range. The minimum possible power was determined by plasma stability: 2.5 kW for H_2 and 2 kW for D_2 . The maximum power for these experiments was limited by thermal loads on the device. A measurement at 5 kW was performed in H_2 , and resulted in damage to the target. The scan in D_2 was therefore limited to 3.5 kW.

3.1. Radiance calculation

The absolute radiance is computed from the acquired spectra. The light from each optical fibre is imaged by the spectrometer into a region of interest (ROI) on the CCD. Nineteen

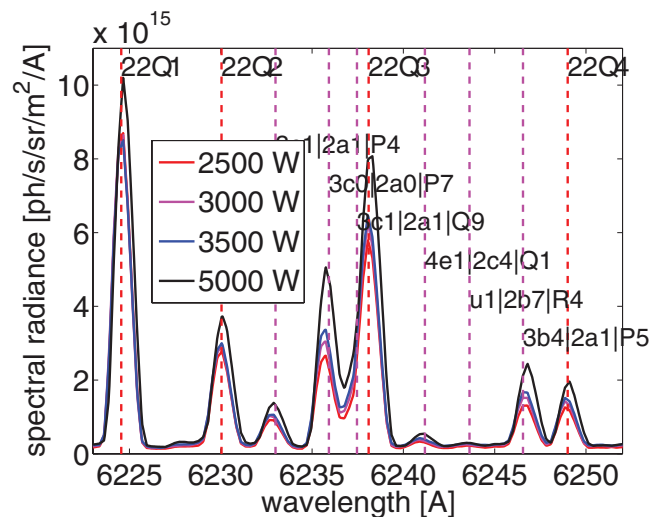


Figure 3. H_2 spectrum of Fulcher- α 22QN lines for different RF powers.

ROIs of approximately 20 vertical pixels are defined. The remaining section of the CCD that is not illuminated was used for CCD-shift smear correction. The photon rate R_{exp} (photons s^{-1}) of each emitted line for each ROI is evaluated using a multi-Gaussian fitting procedure that included the measured experimental instrumental function. The photon rate of lines that are partially overlapped was still computed with satisfactory accuracy. The radiant flux reaching the sensor ϕ_{expt} (W) can be calculated from the photon rate using the equation

$$\phi_{\text{exp}} = R_{\text{exp}} h\nu_{\text{ph}}, \quad (1)$$

where ν_{ph} is the photon frequency and h is the Planck constant. The absolute radiance is then deduced by comparing the experimental rate R_{exp} with the photon rate R_{cal} measured with an absolutely calibrated source at the same wavelength, using the same experimental configuration. This ensures correct compensation for the system transmission and geometrical etendue. The radiance L_{exp} (photons $\text{s}^{-1} \text{ sr}^{-1} \text{ m}^{-2}$) of a line is given by

$$L_{\text{exp}} = \frac{R_{\text{exp}}}{R_{\text{cal}}} L_{\text{cal}} \quad (2)$$

where L_{cal} is the known spectral radiance of the calibration source integrated over the pixel wavelength range. An example of an H_2 molecular spectrum in the range of the 22QN (with $N = 1$ – 4) lines is shown in figure 3, where the molecular lines are identified from reference wavelengths in Dieke [15]. The same procedure is implemented for D_2 using the reference lines in Lavrov's atlas [16]. Figures 4 and 5 show the resulting radiance profiles for the first three Balmer lines and the molecular 22Q1 line, for H_2 and D_2 respectively. Each line has a characteristic radiance profile shape that is independent of the input RF power, which only determines the absolute radiance value. There is also a noticeable isotope effect on both profile shape, broader in deuterium, and radiance level, higher in deuterium for the atomic lines. The radiance of the 22Q1 D_2 line is much lower than that of the 22Q1 H_2 line. This is partially due to the different nuclear spin of the isotopes,

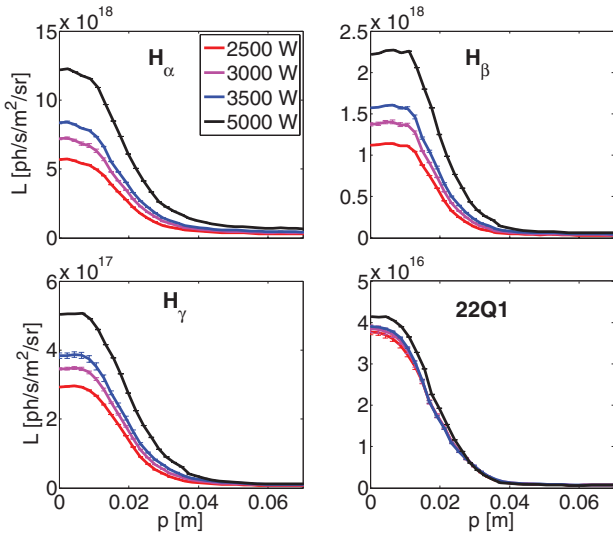


Figure 4. Radiance profiles $L(p)$ of Balmer and 22Q1 lines for H_2 . Different colours indicate different RF powers.

that interchange the statistical weight for even–odd rotational molecular levels [17]. Nevertheless, the total D_2 Fulcher- α Q-branch emission is lower than for H_2 . The radiance of Balmer lines increases linearly with the RF power, while there is no clear dependence for the molecular line radiance.

3.2. Tomographic inversion

A tomographic inversion is then applied to extract the emissivity profiles from the radiance. The inversion of the line-integrated data, in this case the radiances L_j with $j = 1, 2, \dots, n_{\text{LOS}}$, is a well known ill-posed mathematical problem, as the system of integral equations for the emissivity ϵ

$$L_j = \int_{\text{LOS}_j} \epsilon \, dl \quad (3)$$

is under-determined. To make it treatable, further conditions must be applied [18]. This is increasingly problematic with a limited number of LOS, as is the case for the measurements reported here. In comparison, in medical tomography, about 10^5 LOS are routinely used. An important improvement for accurate Abel tomographic inversion is having multiple observation positions, not possible with RAID due to diagnostic access limitations at the time of the experiment. This requirement can be relieved in cases where the object has symmetry properties and, as mentioned above, the RAID plasma column has cylindrical symmetry. The chosen approach was to subdivide the cross section into n_r radially concentric pixels of constant emissivity ϵ_i , $i = 1, 2, \dots, n_r$ and recast the integral problem as a system of algebraic equations in matrix formalism:

$$\epsilon_i = T_{ij} L_j \quad (4)$$

where the element T_{ij} of the transfer matrix T is the intersection length of the LOS j with the pixel i . The transfer matrix size is $n_r \times n_{\text{LOS}}$. A unique solution of system (4) can be found by choosing $n_r < n_{\text{LOS}}$ and imposing a further regularization on the solution, achieved by minimizing the functional

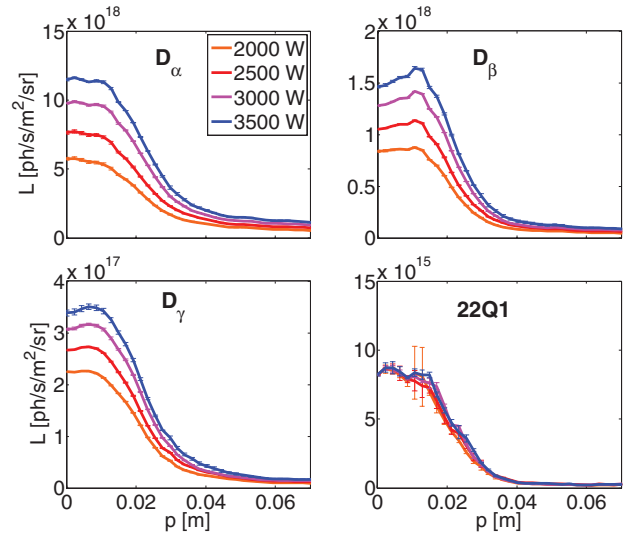


Figure 5. Radiance profiles $L(p)$ of Balmer and 22Q1 lines for D_2 . Different colours indicate different RF powers.

$$\tilde{h} = \frac{1}{2} \chi^2 + \alpha \mathcal{R}. \quad (5)$$

The positive parameter α acts as a weighting factor between the regularizing functional \mathcal{R} and a least-squared optimized fitting. A desirable property for the regularization is to perform a strong smoothing when the emissivity is low yet allow larger variations when the emissivity is high, to better distinguish features in the luminous core region. The Fisher information,

$$I_f = \int \frac{\left(\frac{d\epsilon(l)}{dl}\right)^2}{\epsilon} dl \quad (6)$$

has this property [19], and was chosen as the regularizing functional. The implemented algorithm, called the minimum Fisher regularization method [20], solves the system of normal equations, equivalent to minimizing the functional of equation 5,

$$(T^T * T + \alpha \tilde{H}) * \epsilon = T^T L \quad (7)$$

where the \tilde{H} matrix contains the Fisher information. The parameter α is optimally chosen by the algorithm. Appropriate convergence of the algorithm is verified by reconstructing the input radiance profiles from the output emissivities and comparing with the initial data. A value $n_r \leq n_{\text{LOS}}$ is selected to preserve as many of the smaller features as possible in the inverted profile. Particular care must be taken in choosing the boundary conditions. Measurements were limited to the impact parameter $p_{\text{max}} \sim 8$ cm, where the radiance has yet to vanish; a straightforward inversion thus yields a non-physical spike in the emissivity profile at this position. The correction of this feature required an extrapolation of the radiance profile, before the inversion, to the unknown zero radiance point p_0 . Several extrapolation methods were tested, linear, quadratic and exponential, to choose p_0 . The resulting emissivities are thus robust against variations of the extrapolating methods and p_0 position, with an uncertainty within 25% at p_{max} , decreasing to less than 10% at 6 cm, for impact parameters

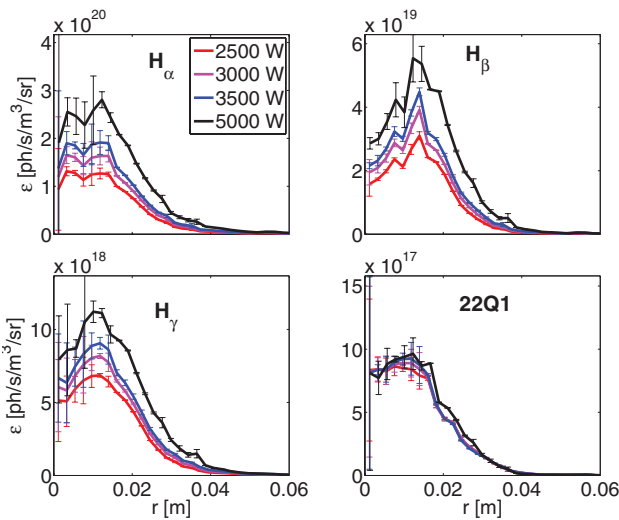


Figure 6. Emissivity profiles $\epsilon(r)$ of Balmer and 22Q1 lines for H_2 . Different colours indicate different RF powers.

of p_0 in the range 16–20 cm. From these assessment results, a linear extrapolation with p_0 at 20 cm was chosen for all the inversions as the lowest-order, and thus more stable, approach. An uncertainty estimate of the Abel-inverted profiles was performed using a Monte Carlo approach [21]. For each radiance profile a set of 400 virtual profiles was generated, varying the radiance value at each position according to a normal distribution centred at the original profile value, with a standard deviation given by the computed uncertainty. Each of these virtual profiles was then inverted using the methods described above, with the emissivity uncertainty taken as the standard deviation of the virtual emissivity profiles. The average value of the virtual profiles was verified to converge to the inversion of the original profile.

Figures 6 and 7 show the computed emissivity profiles and their uncertainties for the Balmer lines and the molecular 22Q1 line, for H_2 and D_2 , respectively. Emissivity profiles are generally hollow and their shape is preserved for different input powers. The hollowest profile is for the Balmer β line (for both H_2 and D_2), which is a consequence of the already hollow radiance profile. The Balmer α line is only slightly hollow and, considering the estimated uncertainties, remains compatible with a flat profile. The molecular line profiles are also slightly hollow, with a similar behaviour as the H_α line. The estimated uncertainties from the Monte Carlo assessment provide a high confidence in the inverted profiles in the 1.5–6 cm radial range, where their values are typically $\leq 15\%$.

4. Analysis with YACORA code and power scan results

Now that the experimental emissivity profiles have been measured and their uncertainties estimated, we seek to deduce the ion population profiles in the RAID plasma. The radial profiles of the first three Balmer lines and the sum of the diagonal Fulcher- α lines are interpreted using the collisional–radiative (CR) code YACORA [22]. This code solves the CR

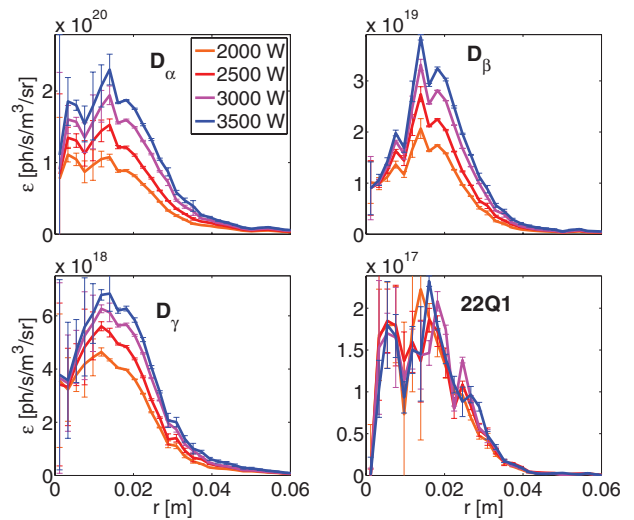


Figure 7. Emissivity profiles $\epsilon(r)$ of Balmer and 22Q1 lines for D_2 . Different colours indicate different RF powers.

rate equations for the population density n_s of the H atom, resolving the lower 40 energy states ($s = 1, 2 \dots 40$). The reactions included in the model are: excitation and de-excitation by e^- collisions, spontaneous emission, ionization, recombination (radiative, dielectronic and three-body) of H^+ , dissociative excitation of H_2 , dissociative recombination of H_2^+ and H_3^+ and mutual neutralization of H^- with H^+ , H_2^+ and H_3^+ . When available, cross sections are preferred to rate coefficients, which gives YACORA the ability to perform calculations with non-Maxwellian EEDF. The reported analysis was performed assuming a Maxwellian EEDF. YACORA is able to include effects due to opacity, but these are neglected in the current analysis since they are expected to be negligible at the low plasma density of these experiments [23]. The densities of the six species H , H^- , H_2 , H^+ , H_2^+ and H_3^+ are varied independently, together with the electron density n_e and temperature T_e , for each code run and are then compared with the measured emissivity, with a trial and error procedure. When the deviation from the experimental value is lower than 10% a match is determined. The use of H_2^+ and H^- is mandatory to reach convergence. This implies that other, simpler, OES analysis methods, which neglect some of the species considered by YACORA, could lead to erroneous estimations if the excluded channels are important [24]. In these plasmas, the mutual neutralization channel of H^+ is fundamental in the analysis while the H^+ recombination channel is essentially irrelevant. Uncertainties of 20% are assigned to the electron density and temperature according to results from code validation in similar low-pressure plasmas [22]. The uncertainty on the density ratio of atoms to molecules is given by the uncertainty of the corresponding emissivities, as the ratio of the rate coefficients is insensitive to T_e and n_e . For this reason an upper limit for uncertainty of 20% is chosen. The uncertainty for the other species (H^- , H^+ , H_2^+ and H_3^+) depends strongly on the contribution of the corresponding process to the Balmer line radiation. In this case an estimated upper limit to the uncertainty of 40% is applied. For this paper, the procedure was time-consuming

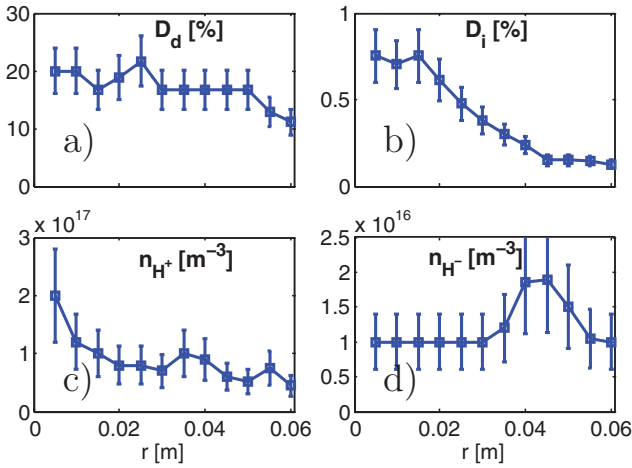


Figure 8. Profiles of (a) degree of dissociation D_d , (b) degree of ionization D_i , (c) H^+ density and (d) H^- density estimated by YACORA for an input power of 3 kW in hydrogen.

and was performed manually; so only a reduced set of three radial positions (at 1.5, 3 and 4 cm) was considered for analysis. These positions were chosen from the results of the 3 kW RF power in hydrogen, which was the only case for which the full profile was completed, as detailed below.

Figure 8 shows the degree of dissociation, the degree of ionization and the H^+ and H^- density profiles estimated by YACORA for this latter case. The degree of dissociation D_d is defined as

$$D_d = \frac{f}{f+2} \quad (8)$$

with f the ratio of atomic to molecular density and is approximately constant for radii smaller than 5 cm, with values larger than 15%. The degree of ionisation D_i , defined as

$$D_i = \frac{n_e}{n_H + n_{H_2}}, \quad (9)$$

is peaked in the core region, $r \leq 1.5$ cm, where it almost reaches 1%. It decreases linearly with radius by one order of magnitude at 4.5 cm, remaining constant at larger radii. The H^+ density is strongly peaked on-axis for $r < 1$ cm, while the negative ion density has a peak in the edge region between 4 and 5 cm. The radial position 1.5 cm is representative of the core region, the 3 cm point is a transition region for both n_{H^+} and n_{H^-} and the final position at 4 cm is where the negative ion density peaks. The n_e and T_e profiles determined via YACORA are compared in figure 9 with experimental profiles measured with an RF-compensated Langmuir probe (LP), by integrating the EEDF. A voltage sweep of $[-60, +35]$ V was used in order to characterize the $I-V$ curve. The T_e profile is in agreement but there remains a discrepancy of about a factor of two in the n_e profile in the core region that is still under investigation. Nevertheless the hollow electron density profile measured by the LP probe is in agreement with the hollow emissivity profiles. The gas translational and vibrational temperatures are estimated from Boltzmann plots of the Fulcher lines [25] and are respectively $T_{\text{tran}} = 900 \pm 200$ K and $T_{\text{vib}} \geq 6000 \pm 1000$ K for the first five vibrational levels in the ground state. These

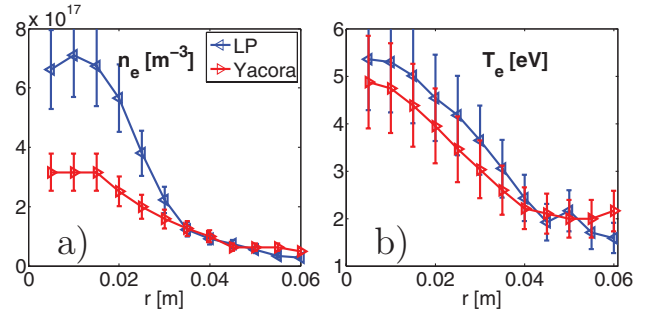


Figure 9. Comparison of experimental (a) n_e and (b) T_e profiles (LP) with YACORA convergence values for input power 3 kW in hydrogen.

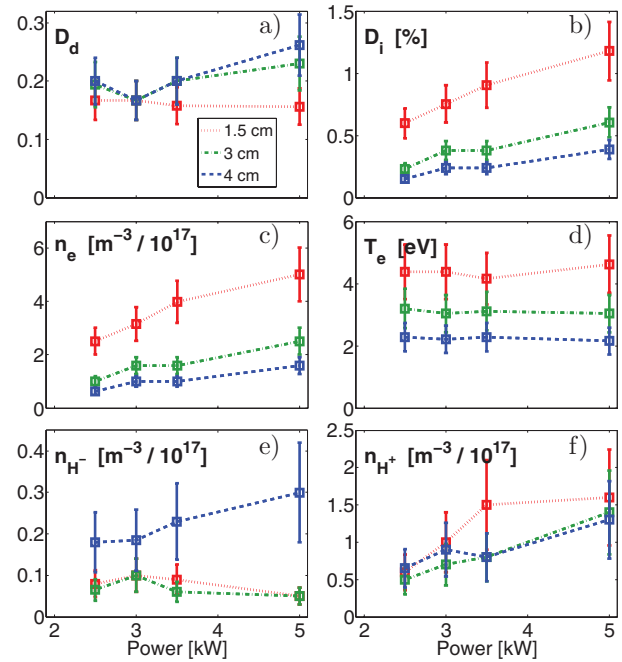


Figure 10. Results of YACORA analysis for power scans in hydrogen H_2 at radial positions 1.5, 3 and 4 cm, as function of input power: (a) degree of dissociation D_d , (b) degree of ionization D_i , (c) n_e , (d) T_e , (e) n_{H^-} and (f) n_{H^+} .

values are found not to depend upon input power and remain constant at all radii.

Figures 10 and 11 show the results of the analysis for hydrogen and deuterium, respectively, at the three radial position considered, as a function of the input power, and clearly display the isotope effect. For the same conditions, the degree of dissociation and the ion densities are larger for deuterium than for hydrogen, while electron temperatures are lower. Trends with power are generally similar for both isotopes. Both n_e and T_e are decreasing functions of the radius, as already seen in figure 9, but while n_e increases linearly with input power, T_e is almost insensitive at all positions. Being able to increase the plasma density without increasing the temperature is a typical feature of helicon sources, and is highly desirable for a negative ion source for NB, as it would permit an easy tuning of the negative ion production rate. The degree of dissociation slightly increases with power and with the radius, reaching 35% and

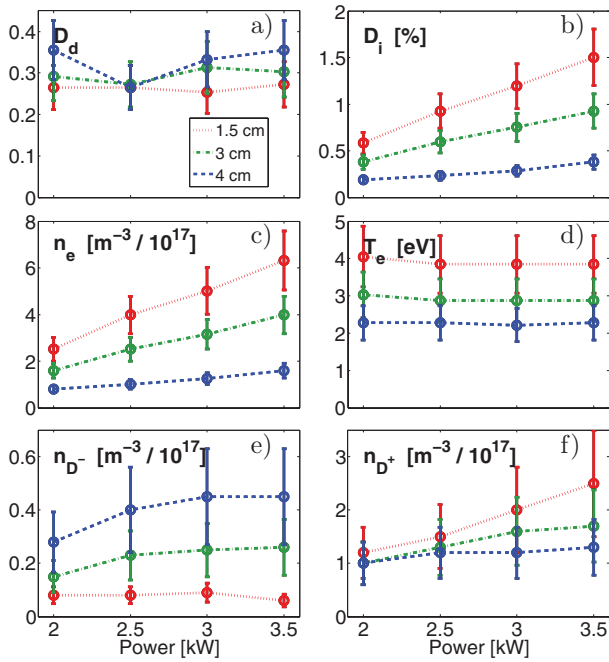


Figure 11. Results of YACORA analysis for power scans in deuterium D₂ at radial positions 1.5, 3 and 4 cm, as function of input power: (a) degree of dissociation D_d , (b) degree of ionization D_i , (c) n_e , (d) T_e , (e) n_{D^-} and (f) n_{D^+} .

25% at 4 cm for deuterium and hydrogen, respectively. The weak dependence of the degree of dissociation on position could be explained by the hydrogen mean free path, which is estimated to be a few centimetres. The neutral hydrogen atoms are generated by dissociation in the core region, where T_e and n_e are high, and diffuse to larger radii. The flat neutral density profile is related to a relatively large mean free path compared with the observation volume. The positive H⁺ ions exhibit the same behaviour as n_e , but with lower values, H₂⁺ and H₃⁺ (not shown) ensuring quasi-neutrality. The negative ion density is relatively low and insensitive to the input power inside the plasma column (radius < 3 cm), where the relatively high T_e reduces stable H⁻ formation and lifetime. At the edge of the plasma column, for $r \geq 4$ cm, the negative ion density attains high values of strong interest for a negative source development. The trend at 4 cm is different between the two isotopes (see figures 10(e) and 11(e)). For hydrogen, the negative ion density increases linearly with power, reaching $3 \times 10^{16} m^{-3}$ at 5 kW, while for deuterium it saturates to $4.5 \times 10^{16} m^{-3}$ at 3 kW, with a similar trend, but lower values, at 3 cm.

5. Discussion

The results shown above are extremely encouraging for the application of the helicon antenna as a negative ion source in the Cybele configuration, which exploits an extremely elongated extraction geometry. The degree of dissociation D_d reaches relevant values for surface production at all the powers of the scan. The degree of ionisation D_i , which directly determines the ability to extract negative ions from a source, is a

limiting factor at these input powers. However, the application of this plasma source for surface production is still feasible (in both H₂ and D₂) if the linear increase in D_i is maintained at higher powers.

The scan in power, for this paper, was interrupted at 5 kW following damage assessment on the machine during hydrogen operation. Furthermore, the antenna matching box was not compatible with higher powers. A new matching box and improvements on the chamber cooling system were designed and are now in the commissioning phase, to extend the exploitation of the antenna to its full potential.

A first analysis of the possible application of this antenna as a volumetric source is presented. Direct extraction and acceleration of the negative ions surrounding the plasma column should be feasible without the positive ion flux which is essential for surface production. The limiting factor in this case is the maximum attainable negative ion density and the ratio n_{H^-}/n_e , which is directly related to the co-extracted electron fraction. The negative ion density has contrasting trends for the two isotopes tested. In deuterium it appears close to saturation, while for hydrogen it retains a linear dependence so that extrapolation at higher powers remains unclear. The ratio of negative ions to electron density is likely to decrease with power from the deduced values of about 0.3, whereas the required ratio should be higher than one. It is possible that this behaviour can be corrected by modifying the magnetic configuration and an extensive study will be necessary to assess this possibility.

6. Conclusions and outlook

OES measurements were performed in RAID to characterize the performance of a newly developed resonant network helicon antenna. Absolute emissivity profiles for the first three Balmer lines and the molecular diagonal Fulcher- α lines were computed by Abel-inverting multi-channel radiance profile measurements. The emissivities were interpreted using the collisional radiative code YACORA, which provided an estimated density for the six species H, H⁻, H₂, H⁺, H₂⁺ and H₃⁺. The population trends with input power were initially studied at three different radial positions. The results obtained are promising for application of the antenna as a negative ion source if maintained and if extraction and acceleration in a beam source behave as expected on the beam test stand. The plasma is effectively confined in a column along the whole length of the RAID. On the device axis, a high plasma density $n_e \geq 6 \times 10^{17} m^{-3}$ is attained at low input power, with a relatively high electron temperature ≈ 5 eV. At the edge of the plasma column, $r \geq 4$ cm, where the electron density and temperature decrease to $\approx 1 \times 10^{17} m^{-3}$ and ≈ 2 eV respectively, a high degree of dissociation ($\geq 35\%$) and a high negative ion density ($\approx 4.5 \times 10^{16}$) are obtained. It should be noted that these negative ion densities already reach values close to those near the extraction region of caesium negative sources [5]. Extrapolation of these results to a nominal antenna power of 10 kW remains complicated by the large gap between the

upper power in deuterium and the observed isotope dependences. A conservative linear extrapolation of n_e results in a density of $2 \times 10^{18} \text{ m}^{-3}$ for deuterium, corresponding to a degree of ionization of 0.05. This would result in an increase in the negative ion yield with power in applications for surface production, even assuming that the negative ion density due to volumetric production and the degree of dissociation saturate to the values at 3.5 kW input power. To reduce the extrapolation uncertainties, source performance at 10 kW will be verified with a new set of measurements after the commissioning of the chamber cooling system and installation of the new matching box are completed. Increasing the diagnostic array around this new source will allow us to harden these conclusions. In addition to refining the spectroscopic and Langmuir measurements, a photodetachment diagnostic is under development that can independently measure the negative ion density. A helicon antenna-based system may provide the negative ion injectors, considered necessary for fusion reactor development, with a welcome alternative source.

Acknowledgments

This work has been carried out within the framework of the EUROfusion Consortium and has received funding from the Euratom research and training programme 2014–2018 under grant agreement no. 633053. The views and opinions expressed herein do not necessarily reflect those of the European Commission.

References

- [1] Giruzzi G. et al 2015 *Nucl. Fusion* **55** 073002
- [2] Bacal M. and Wada M. 2015 *Appl. Phys. Rev.* **2** 021305
- [3] Simonin A. et al 2015 *Nucl. Fusion* **55** 123020
- [4] Inoue T. et al 2005 *Nucl. Fusion* **45** 790
- [5] Speth E. et al 2006 *Nucl. Fusion* **46** S220
- [6] Carter M.D. et al 2002 *Phys. Plasmas* **9** 5097
- [7] Rapp D. et al 1965 *Phys. Rev. Lett.* **14** 533
- [8] Schulz G.J. 1973 *Rev. Mod. Phys.* **45** 423
- [9] Walton D.S. et al 1971 *J. Phys. B: At. Mol. Phys.* **4** 1343
- [10] Godyak V.A. et al 1992 *Plasma Sources Sci. Technol.* **1** 36
- [11] Siddiqui U.M. et al 2015 *Plasma Sources Sci. Technol.* **24** 015022
- [12] Chen F.F. 1995 1—Helicon plasma sources *High Density Plasma Sources* ed O. A. Popov (Park Ridge, NJ: William Andrew Publishing) pp 1–75
- [13] Guittienne Ph., Chevalier E. and Hollenstein Ch. 2005 *J. Appl. Phys.* **98** 083304
- [14] Bell R.E. and Scotti F. 2010 *Rev. Sci. Instrum.* **81** 10D731
- [15] Dieke G.H. 1972 *The Hydrogen Molecule Wavelength Tables of G. H. Dieke* ed H.M. Crosswhite, The Johns Hopkins University (New York: Wiley-Interscience)
- [16] Lavrov B.P. and Umrikhin I.S. 2016 *J. Quant. Spectrosc. Radiat. Transfer* **182** 180–192
- [17] Farley D.R. et al 2011 *J. Quant. Spectrosc. Radiat. Transfer* **112** 800
- [18] Carey C.S. et al 2004 *Rev. Sci. Instrum.* **75** 3411
- [19] Furno I. et al 2001 *Nucl. Fusion* **41** 403
- [20] Anton M. et al 1996 *Plasma Phys. Control. Fusion* **38** 1849
- [21] Bortolon A. et al 2013 *Nucl. Fusion* **53** 023002
- [22] Wunderlich D., Dietrich S. and Fantz U. 2009 *J. Quant. Spectrosc. Radiat. Transfer* **110** 62–71
- [23] Behringer K. and Fantz U. 2000 *New J. Phys.* **2** 23
- [24] Fantz U. and Wunderlich D. 2006 *New J. Phys.* **8** 301
- [25] Cameron M.S. and Cormac S.C. 2015 *Plasma Sources Sci. Technol.* **24** 045003